



## ORIGINAL RESEARCH ARTICLE

## Patterns and wavelet coherence analysis of tidal dynamics and chlorophyll a concentration

M.N. Hidayat<sup>1</sup>, R. Wafdan<sup>2</sup>, M. Ramli<sup>2</sup>, Z.A. Muchlisin<sup>1,3,5</sup>, S. Rizal<sup>1,4,5,\*</sup><sup>1</sup> Graduate School of Mathematics and Applied Sciences, Universitas Syiah Kuala, Banda Aceh 23111, Indonesia<sup>2</sup> Department of Mathematics, Universitas Syiah Kuala, Banda Aceh 23111, Indonesia<sup>3</sup> Department of Aquaculture, Faculty of Marine and Fisheries, Universitas Syiah Kuala, Banda Aceh 23111, Indonesia<sup>4</sup> Department of Marine Sciences, Faculty of Marine and Fisheries, Universitas Syiah Kuala, Banda Aceh, 23111, Indonesia<sup>5</sup> Research Center for Marine Sciences and Fisheries, Universitas Syiah Kuala, Banda Aceh 23111, Indonesia

## ARTICLE INFO

## Article History:

Received 16 October 2023

Revised 19 November 2023

Accepted 30 January 2024

## Keywords:

Chlorophyll a

Semidiurnal tides

SH parameter

Tidal mixing Water column mixing

Wavelet transform coherence

## ABSTRACT

**BACKGROUND AND OBJECTIVES:** Understanding the correlation between tidal rhythms and marine organism behavior is crucial. This extends beyond fluctuations in chlorophyll a concentrations and includes various biological processes in the marine environment. Awareness is key for a comprehensive perspective on the role of tidal forces, affecting ocean's physical aspects and life form diversity. This study aims to explore the complex relationship between tidal movements and chlorophyll a concentrations in the northern Bay of Bengal, focusing on how tidal rhythms affect chlorophyll a concentrations.

**METHODS:** The analyzed variables include tidal parameters, such as lunar semidiurnal tidal characteristics and Simpson–Hunter parameters, as well as sea level, tidal current, and current magnitude, obtained from the Tidal Model Driver. Additionally, hourly chlorophyll a data for January 2022 were acquired from the geostationary meteorological satellite Himawari-8, and the rate of change of chlorophyll a was determined through chlorophyll a calculations. This study employs wavelet analysis, applying continuous wavelet transform and wavelet transform coherence for chlorophyll a, rate of change of chlorophyll a, sea level, tidal current, and current magnitude, to explore oscillation patterns and temporal correlations within the marine ecosystem of the northern Bay of Bengal.

**FINDINGS:** Lunar semidiurnal tidal amplitudes increase toward the north, peaking at the Sagar and Ramree Islands, and tidal phases rise from south to northeast. Most of the bay, categorized by <0.25 Formzahl values, experiences semidiurnal tides. Surface lunar semidiurnal elliptic currents, stronger in the north and east, flow clockwise and turn counterclockwise toward the south. The Simpson–Hunter parameter indicates heightened tidal mixing, particularly along the northern and eastern coasts. Region 2 showed the highest mean chlorophyll a concentration (12.58 milligram per cubic meter), whereas Region 1 showed the lowest mean chlorophyll a concentration (0.79 milligram per cubic meter). Similar trends were observed for tidal current and current magnitude. The continuous wavelet transform analysis provides data on chlorophyll a and the rate of change of chlorophyll a within 6, 12, and 24 hours, sea level changes within 8–16 hours, and consistent tidal effects on tidal current and current magnitude in the range of 5–7 hours. The wavelet transform coherence analysis highlights the relationships between chlorophyll a and sea level over 12 and 24 hours periods and between chlorophyll a and current magnitude. Furthermore, the wavelet transform coherence analysis examines the rate of change in chlorophyll a in relation to tidal currents over 6, 12, and 24 hours.

**CONCLUSION:** Tides remarkably affect chlorophyll a concentrations. There are strong links between chlorophyll a concentrations and key tidal aspects, such as sea level and current magnitude. Higher tidal variables correlate with increased chlorophyll a concentrations and are related to the Simpson–Hunter parameter, indicating that regions with vigorous mixing show higher chlorophyll a concentrations. This finding highlights the major role of tidal forces and variations in the chlorophyll a concentrations in the Bay of Bengal. The wavelet transform coherence analysis of chlorophyll a, sea level, and current magnitude data in Regions 1, 2, and 3 show notable coherence in all areas.

DOI: 10.22035/gjesm.2024.03.\*\*\*

This is an open access article under the CC BY license (<http://creativecommons.org/licenses/by/4.0/>).

NUMBER OF REFERENCES

45



NUMBER OF FIGURES

5



NUMBER OF TABLES

2

\*Corresponding Author:

Email: [srizal@usk.ac.id](mailto:srizal@usk.ac.id)

Phone: +628 52571 49009

ORCID: 0000-0003-3637-2351

Note: Discussion period for this manuscript open until October 1, 2024 on GJESM website at the "Show Article".

## INTRODUCTION

According to [Xing et al. \(2021\)](#), tides play a crucial role as hydrodynamic forces in continental shelf seas, significantly influencing marine ecosystems and biogeochemical cycles. The spring–neap tidal cycle has been observed to lead to biweekly variations in chlorophyll *a* (Chl-*a*) concentrations in certain shelf waters. A significant obstacle in investigating these phenomena is the prevalence of missing data and the infrequency of satellite observations. The biweekly variations in Chl-*a* concentrations are strongly associated with the differences in tidal currents (TC) observed during spring and neap tides. Furthermore, these differences in TC are instrumental in determining the seasonal effects of spring–neap tides on Chl-*a*, particularly in temperate coastal regions. Gaining insights into the effects of short-term hydrodynamic processes on Chl-*a* in marine ecosystems is key to a more profound understanding of ecosystem dynamics and biogeochemical cycles. The concentration of phytoplankton biomass, often quantified in terms of Chl-*a*, is crucial for understanding various environmental issues. Chl-*a*, the primary molecule responsible for photosynthesis, serves as an indicator of water quality and a proxy for biomass content ([Boyer et al., 2009](#)). High Chl-*a* concentrations can indicate eutrophication, which leads to harmful algal blooms that affect aquatic ecosystems, water quality, and marine life. Conversely, low Chl-*a* concentrations can indicate limited biological activity, potentially impacting the marine food web and carbon cycling. Thus, monitoring Chl-*a* concentrations helps in assessing and managing these environmental concerns. Tides, commonly recognized as the primary hydrodynamic force on most continental shelves, have a notable influence on the dynamics of marine ecosystems. This influence has been extensively investigated and documented. For instance, [Shi et al. \(2013\)](#) analyzed the tidal effects on ecosystem variability in the Chesapeake Bay, whereas [Eleveld et al. \(2014\)](#) examined the impact of tidal and meteorological factors on estuarine suspended particulate matter concentrations. These studies collectively underscore the significant influence of tidal cycles, particularly spring–neap tidal cycles, on Chl-*a* fluctuations. This significant tidal impact is also evident in the in situ observations. [Van der Hout et al. \(2017\)](#) investigated the dynamics of suspended particulate matter and

Chl-*a* from intratidal to annual timescales in a coastal turbidity maximum. Furthermore, [Li et al. \(2021\)](#) explored tidally induced temporal variations in the growth of young-of-the-year Pacific cod in the Yellow Sea. These studies collectively underscore a significant correlation between the tidal rhythms and the behavior of marine organisms. This intricate relationship emphasizes the importance of understanding how tides affect marine ecosystems, extending beyond fluctuations in Chl-*a* concentrations to include a broader range of biological processes in these environments. This comprehension is essential for a comprehensive view of the role of tidal forces, illustrating how they influence not only the chemical and physical aspects of the oceans but also the myriad of living entities that inhabit these waters. Such knowledge is invaluable for a complete understanding of marine ecosystems, providing insights into the interconnectedness of physical forces and biological life in the oceanic realm. The influence of tidal oscillations on marine biological processes is intricate and diverse, playing a pivotal role in shaping the vertical stability of the water column, the distribution of nutrients, and the development of phytoplankton. These elements are crucial for the structure and functionality of marine ecosystems. Tidal oscillations create a cycle of intense tidal mixing and substantial stratification, each impacting the vertical stability of the water column in distinct ways. This fluctuation affects the physical and chemical attributes of water, consequently influencing vital biological processes. The condition of the water column is of paramount importance for phytoplankton growth. During periods of high tidal energy with pronounced vertical mixing, essential nutrients are carried to the surface layer, fostering photosynthetic growth, as explored by [Cullen and Lewis \(1988\)](#) in their study on algal photoadaptation in the context of vertical mixing and by [Demers et al. \(1986\)](#) in their research on phytoplankton responses to vertical tidal mixing. Nonetheless, this same process can transport phytoplankton below the photic layer, impairing their growth because of diminished light exposure, as investigated in the studies conducted by [Lagadeuc et al. \(1997\)](#) on the temporal variations in the vertical stratification in a tidal region of a freshwater influence system and by [Lauria et al. \(1999\)](#) on the contrasting phytoplankton distributions controlled by tidal turbulence in an estuary. Periods of high tidal energy

are instrumental in delivering nutrients to the surface layer via turbulent processes and diffusion, which are vital for the sustenance of photosynthetic organisms, as highlighted by [Sharples et al. \(2007\)](#). Conversely, during periods of low tidal energy, the surface layer is depleted of nutrients, and fewer organisms are displaced from the photic layer, leading to restratification. This change fosters a diverse array of environmental conditions that distinctly affect marine life. The continuous alternation of these contrasting environmental conditions, driven by tidal oscillations, significantly influences the overall structure and dynamics of the marine ecosystem, as noted by [Cadier et al. \(2017\)](#). The northern Bay of Bengal (NBoB) is an area with abundant fish and is a significant contributor to global fish production ([FAO, 2011](#)). [Raju et al. \(2022\)](#) reported that fishing is concentrated in a small region of the continental shelf, particularly between the 10 m and 50 m depth contours. Local fishing communities, who possess knowledge of the ocean and its behavior, are already familiar with these areas of high fish concentration. According to [Madhuratap et al. \(2003\)](#), the NBoB is unique because of its coastlines, marine features, and ecological relationships. This area is also affected by frequent storm surges and tides, which cause significant changes in sea level (SL) over time, as noted by [Tazkia et al. \(2017\)](#). The climate in the NBoB is mainly influenced by monsoons, which are seasonal winds. The northeast (NE) monsoon usually occurs from November to February, and the southwest monsoon occurs from June to September, as described by [Goswami et al. \(2016\)](#). Wind pressure and speed are stronger in August than in February, according to [Hidayat et al. \(2023\)](#). The research conducted by [Díez-Minguito and de Swart \(2020\)](#) in the Guadalquivir estuary showed that, on a tidal timescale, Chl-*a* concentrations exhibit synchronized fluctuations in line with the spring–neap tidal cycle. Peak Chl-*a* concentrations were observed during periods of maximum ebb and flow. Furthermore, the highest Chl-*a* concentrations were typically recorded 2–3 days following a neap tide. This delayed response could be linked to a complex interplay of various factors, potentially including the availability of light and the influence of sedimentation, as noted by [Azhikodan and Yokoyama \(2016\)](#). In this study, the relationship between Chl-*a* concentrations and tidal movements is examined. To achieve this objective, a

broad investigation of tidal patterns in the NBoB was first undertaken. This involved determining the amplitude and phase of lunar semidiurnal (M2) tides, calculating the Formzahl number (*F*) to classify the tidal patterns of the NBoB, examining the elliptical surface layer currents during M2 tides, and analyzing the Simpson–Hunter (SH) parameter of M2 TC. Subsequently, an analysis of hourly Chl-*a* data from January 2022 was conducted, comparing it and its rate of change (calculated as the derivative of the natural logarithm of Chl-*a* with respect to time) with various tidal variables. These variables included SL elevation, TC, and current magnitude ( $|U|$ ) data, all recorded during the same period in January 2022. The analysis led to several descriptive conclusions. The impact of the SH parameter on the variability of Chl-*a* concentrations was investigated by categorizing three regions based on the SH parameter values. Region 1 has high SH parameter values, indicating low tidal dynamics, whereas Region 2 has low SH parameter values, indicating high tidal dynamics. Region 3 has moderate SH parameter values. The period of each time series of each variable related to Chl-*a* and tides is determined through continuous wavelet transform (CWT) analysis. In addition, a quantitative relationship between Chl-*a* concentrations and tidal variables was established through wavelet transform coherence (WTC) analysis. Analyzing the relationship between Chl-*a* and tides is crucial because of the profound impact of tides on marine ecosystems and marine biological processes. Tides, as primary hydrodynamic forces, induce biweekly variations in Chl-*a* concentrations in coastal waters during spring–neap tidal cycles, influencing short-term processes in marine ecosystems. For example, [Shi et al. \(2011\)](#) examined the tidal effects on satellite ocean color observations, whereas [Roden \(1994\)](#) investigated Chl-*a* blooms and tidal patterns. [Sharples et al. \(2007\)](#) explored internal tide mixing, and [Koh et al. \(2006\)](#) reported higher Chl-*a* concentrations during spring tides. Understanding this relationship extends beyond physical and chemical aspects, impacting the behavior and growth of marine organisms, as reported by [Rahman and Cowx \(2006\)](#) and [Krumme et al. \(2008\)](#). In regions such as the NBoB, where fishing is vital, recognizing these patterns is crucial for sustainable practices and ecosystem management. This knowledge aids in predicting fish behavior and maintaining fish stocks.

In the NBoB, which is characterized by unique features and ecological relationships, analyzing Chl-*a* and tides is vital. Research, as exemplified by Díez-Minguito and de Swart (2020), reveals synchronous Chl-*a* fluctuations with the spring–neap tidal cycle, which is essential for understanding different factors, such as light availability and sedimentation in the marine ecosystem. This knowledge promotes effective environmental management and sustainability in the NBoB. Numerous studies have been conducted on Chl-*a* in the NBoB. Raju *et al.* (2023) explored the spatial and temporal variations in the thermal front in this region and its interaction with Chl-*a* concentrations around fishing vessel clusters on the continental shelf and determined that these thermal fronts, present on the continental shelf and at the shelf break, exhibit notable persistence and a strong seasonal pattern, primarily driven by annual cycles. To identify these thermal fronts, Raju *et al.* (2023) employed the moderate resolution imaging spectroradiometer daily sea surface temperature (SST) along with the weekly Chl-*a* concentration data. In a separate study, Hidayat *et al.* (2023) investigated the relationship between Chl-*a*, SST, and sea surface salinity using monthly time series data but did not establish a correlation between Chl-*a* and tides. Meanwhile, Poddar *et al.* (2019) focused solely on estimating the Chl-*a* concentration in the northern coastal areas of the Bay of Bengal, without linking it to tidal influences. Naderipour *et al.* (2021) determined the best setup for hybrid renewable energy systems, focusing on the role of tidal energy, and emphasized the substantial impact of tidal energy in certain regions, increased use of photovoltaic energy in one area, and reduced dependence on wind turbine sources. These findings underscore the significance of incorporating tidal energy into these systems. Koropitan *et al.* (2022) examined the effects of Cyclone Marcus on oceanographic processes within both the subsurface and surface layers, along with its implications for temperature and Chl-*a* concentrations in the Southeastern Indian Ocean. This investigation uses data from the Copernicus dataset and Argo floats to thoroughly analyze the oceanographic characteristics of the region before, during, and after the occurrence of Cyclone Marcus. Importantly, the aforementioned studies do not assess the relationship between Chl-*a* and tides. The present study takes a distinct path by investigating

the relationship between Chl-*a*, rate of change of chlorophyll *a* (ROCChl-*a*), and tidal variables, such as SL, TC, and  $|U|$ . To the best of our knowledge, this specific aspect has not been previously explored. Moreover, this study incorporates hourly time series data for both tides and Chl-*a*, providing a more detailed and comprehensive analysis of these environmental factors. This study explores the relationship between tidal movements and Chl-*a* concentrations in the NBoB. This study was conducted at the Ocean Modelling Laboratory, Department of Marine Sciences, Universitas Syiah Kuala, Indonesia, and in the NBoB using the data from 2022.

## **MATERIALS AND METHODS**

This study hypothesizes that tidal movements significantly influence Chl-*a* concentrations in the NBoB, with tidal rhythms correlating with variations in Chl-*a* concentrations and impacting marine organism behavior and ecosystem processes. Based on the aforementioned statements, the following research questions of interest for further exploration have been formulated: (1) What is the distribution pattern of M2 amplitude, M2 phase, tidal type in the NBoB, M2 surface layer elliptic current, and SH parameter? (2) What is the relationship between Chl-*a* and ROCChl-*a* with respect to the following specific tide-related variables: SL,  $|U|$ , and TC? In addition, does the SH parameter influence the Chl-*a* concentrations in this context? (3) What are the periods of the following variables: Chl-*a*, ROCChl-*a*, SL, TC, and  $|U|$ ? (4) How can WTC analysis be used to further explore the interactions and synchronization between Chl-*a* and its ROCChl-*a* with the tide-related variables (SL, TC, and  $|U|$ ) in the NBoB? Question 1 is answered in the section “Tides in the NBoB.” Question 2 is answered in the section “Chl-*a* and tides data,” with a demonstration in Fig. 3. Question 3 is answered in the section “CWT.” Finally, Question 4 is answered in the section “WTC.” The results are shown in Table 2.

### *Study area and data*

The study area is located in the NBoB, spanning the latitude range of 18° N to 23° N and the longitude range of 84° E to 95° E, as illustrated in Fig. 1. Fig. 1 illustrates the depth of the NBoB, highlighting the 10 and 50 m depth contours used by nearby residents for fishing. The growing demand for fish

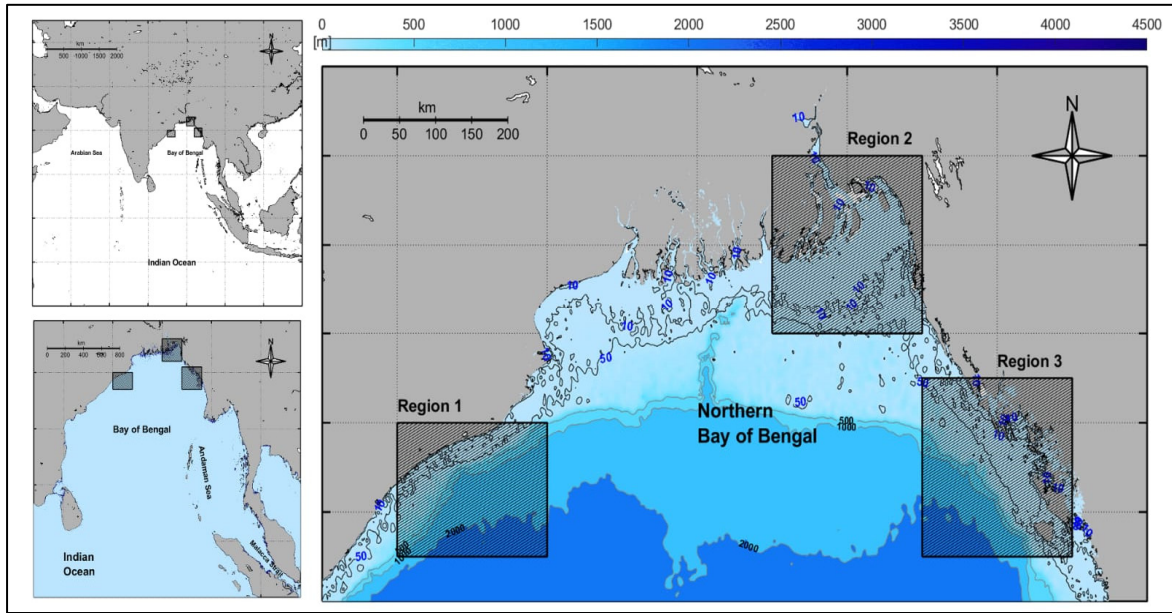


Fig. 1: Geographic location of the study area showing the bathymetry of the NBoB. The data are derived from the Shuttle Radar Topography Mission 15 Plus. Region 1 is located at the coordinates 85° E–87° E and 18.5° N–20° N, Region 2 is located at the coordinates 90° E–92° E and 21° N–23° N, and Region 3 is located at the coordinates 92° E–94° E and 18.5° N–20.5° N. The contours denote the ocean depth (in meters). The thick lines denote the contours of the 10 and 50 m isobaths, which are areas of intense fishing. The color bar denotes the bathymetric depth (in meters), and the scale in the figure is in kilometers.

and unsustainable fishing practices pose the threat of depleting fish stocks, which can have severe consequences for fishing communities and the marine ecosystem. Thus, sustainable fishing practices need to be adopted and this resource needs to be appropriately managed to maintain the productivity of the NBoB and its contribution to global fish production. For further analysis, three regions were selected. The selection of these three regions was based on the SH parameter values. Region 1 has a high SH parameter, Region 2 has a low SH parameter, and Region 3 has a moderate SH parameter value.

The amplitude and phase parameters of the M2 tide, tidal ellipses, and SH parameters were obtained and derived from the Tidal Model Driver (TMD) using the M2 tide component. TMD is a MATLAB package used to access harmonic constituents and make tidal predictions. TMD operates at a resolution of  $1/4^\circ \times 1/4^\circ$  with eight tidal constituents (Padman and Erofeeva, 2005).  $|U|$  is obtained from the  $u$  and  $v$  current components using Eq. 1 (Amsalia et al., 2022):

$$|U| = \sqrt{u^2 + v^2}. \quad (1)$$

SL was discussed in detail by Ikhwan et al. (2021), who used data from the fast Fourier transform. In this study, SL data were obtained from TMD (Padman and Erofeeva, 2005). The TC values were obtained from the SL using Eq. 2 (Blauw et al., 2012):

$$TC \sim \left| \frac{d(SL)}{dt} \right|. \quad (2)$$

Hourly Chl- $a$  data for January 2022 were obtained from the geostationary meteorological satellite Himawari-8, provided by the P-Tree System of the Japan Aerospace Exploration Agency (JAXA) (Murakami, 2016). The ROCChl- $a$  was determined as follows: Initially, data conversion was performed by applying the natural logarithm. This logarithmic conversion decreases skewness and alleviates the

Table 1: Summary statistics of Chl-*a*, ROCChl-*a*, SL, TC, and |*U*| for Regions 1, 2, and 3 in January 2022

Region	Variable	Total Sample	Mean	Median	Min	Max	IQR	Variance	S.D.
1	Chl- <i>a</i>	744	0.79	0.75	0.01	2.24	0.37	0.11	0.33
	ROCCHL	743	0.15	0.13	-0.87	1.30	0.16	0.06	0.25
	SL	744	0.00	0.01	-1.05	1.18	0.87	0.28	0.53
	TC	743	0.22	0.22	0.00	0.54	0.20	0.02	0.13
	<i>U</i>	744	0.04	0.04	0.00	0.09	0.04	0.00	0.02
2	Chl- <i>a</i>	744	12.58	12.80	0.10	25.55	4.52	17.43	4.18
	ROCCHL	743	0.11	0.12	-0.32	0.47	0.08	0.01	0.08
	SL	744	0.00	-0.01	-1.52	1.74	1.39	0.64	0.80
	TC	743	0.35	0.34	0.00	0.78	0.30	0.04	0.19
	<i>U</i>	744	0.81	0.79	0.21	1.58	0.53	0.11	0.33
3	Chl- <i>a</i>	744	1.36	1.33	0.32	3.25	0.40	0.13	0.37
	ROCCHL	743	0.09	0.10	-0.58	0.68	0.26	0.04	0.19
	SL	744	0.00	-0.01	-1.12	1.35	1.01	0.37	0.61
	TC	743	0.26	0.26	0.00	0.61	0.23	0.02	0.15
	<i>U</i>	744	0.24	0.25	0.06	0.44	0.09	0.01	0.07

influence of sporadic high spikes in the Chl-*a* dataset. Subsequently, ROCChl-*a* was computed using Eq. 3 (Blauw et al., 2012):

$$\frac{d \ln(\text{Chl-}a)}{dt} = \frac{1}{(\text{Chl-}a)} \frac{d(\text{Chl-}a)}{dt}. \quad (3)$$

Table 1 summarizes the statistical measures, including the mean, median, minimum value (Min), maximum value (Max), interquartile range (IQR), variance, and standard deviation for Chl-*a*, ROCChl-*a*, SL, TC, and |*U*|.

#### Determining the tidal front

The tidal mixing parameters can be calculated using the SH parameter using Eq. 4 (Simpson and Hunter, 1974):

$$K = \log_{10} \left( \frac{h_0}{u^3} \right), \quad (4)$$

where  $h_0$  is the average water depth (in meters) and  $u$  is the depth-averaged M2 tidal velocity (in meters per second).

#### Wavelet analysis

The CWT, implemented using the Morlet wavelet function, is utilized to detect predominant oscillation patterns and distinct periodic elements within each separate time series. This method provides precise time–frequency resolution, which aids in the

identification of various temporal components. The WTC method is employed to uncover and visually represent intricate time–correlation connections between two sets of data. With its high time–frequency resolution capabilities, WTC helps highlight detailed relationships between the aforementioned data series. The Morlet wavelet function ( $\psi_0$ ) is defined in Eq. 5 (Torrence and Compo, 1998):

$$\psi_0(t) = \pi^{-1/4} e^{i\omega_0 t} e^{-t^2/2}, \quad (5)$$

where  $\psi_0$  is the nondimensional wavelet coefficient,  $i = \sqrt{-1}$ , and  $\omega_0$  is the dimensionless frequency associated with the dimensionless time variable  $t$ , thereby enabling scale resolution adjustment. The formula for CWT with the time series  $X_{\hat{n}}$ ,  $\hat{n} = 1, 2, 3, \dots, N$  and uniform time interval  $\delta_t$  is expressed in Eq. 6 (Grinsted et al., 2004):

$$W_n^X(s) = \sqrt{\frac{\delta_t}{s}} \sum_{\hat{n}=1}^N X_{\hat{n}} \psi_0 \left[ \frac{(\hat{n}-n)\delta_t}{s} \right], \quad (6)$$

where  $\sqrt{\frac{\delta_t}{s}}$  is the normalization factor,  $s$  is the wavelet scale, and  $n$  is the reversed time index. The formula for WTC is expressed in Eq. 7 (Grinsted et al., 2004):

$$R^2(s) = \frac{|S(a^{-1}W_n^{xy}(s))|^2}{S(a^{-1}W_n^x(s)) \cdot S(a^{-1}W_n^y(s))}, \quad (7)$$

where  $W_n^{xy} = W_n^x W_n^{y*}$  is the wavelet cross-spectrum between two signals,  $x_n$  and  $y_n$ . The term  $W_n^{y*}$  is the complex conjugate of  $W_n^y$ .  $S$  is the smoothing operator. The statistical significance level of WTC against red noise or an autoregressive model of order 1 (AR(1)) was determined using the Monte Carlo method (Fu *et al.*, 2012; Grinsted *et al.*, 2004). The phase angle  $\phi_n(s)$  of the WTC is used to analyze the lead-lag connection between two variables and is defined in Eq. 8 (Kristoufek, 2015):

$$\phi_n(s) = \tan^{-1} \left( \frac{\Im \left\{ S \left( a^{-1} W_n^{xy}(s) \right) \right\}}{\Re \left\{ S \left( a^{-1} W_n^{xy}(s) \right) \right\}} \right), \quad (8)$$

where  $\Im$  and  $\Re$  are the imaginary and real part operators, respectively.

## RESULTS AND DISCUSSION

### Tides in the NBoB

Ocean tides consist of a series of sinusoidal and tidal harmonic components unique to each location. The primary components in this sequence are the semidiurnal constituents, i.e., M2, S2, N2, and S2, which have periods of 12.42, 12.00, 12.66, and 11.97 h, respectively. In addition, the diurnal constituents, i.e., K1, O1, P1, Q1, and S1, have periods of 23.93, 25.82, 24.07, 26.87, and 24.00 h, respectively. These varying periods illustrate the complexity and diversity of tidal patterns across different marine environments (Wolanski and Elliott, 2015). Fig. 2a illustrates the tidal amplitude and phase of M2 in the NBoB region. The M2 amplitude exhibits an increasing trend from the southwestern to the northern regions of NBoB, peaking at Sagar Island in the north and Ramree Island in the east, before decreasing again at Cox's Bazar. The highest M2 amplitude was observed at Sagar Island and Ramree Island. In addition, the phase of M2 increases gradually from south to NE in the NBoB. These findings are consistent with those reported by Wan *et al.* (2019). According to Polagye (2009), tidal types are categorized based on the Formzahl number ( $F = (K1 + O1)/(M2 + S2)$ ), where K1 is the amplitude of the diurnal or lunisolar diurnal constituent, O1 is the lunar diurnal constituent, M2 is the semidiurnal constituent, and S2 is the principal solar semidiurnal constituent (Haditjar *et al.*, 2020). The four tidal types are semidiurnal ( $0 < F < 0.25$ ),

mixed and predominantly semidiurnal ( $0.25 \leq F < 1.5$ ), mixed and predominantly diurnal ( $1.25 \leq F < 3.0$ ), and diurnal ( $F \geq 3.0$ ). Fig. 2b shows the  $F$  values for the NBoB, indicating that most of the areas in the bay have  $F < 0.25$ , which corresponds to a semidiurnal tidal type. This result is consistent with the findings of Wan *et al.* (2019), who also reported that semidiurnal tides are prevalent in most of the Bay of Bengal. Fig. 2c shows the M2 elliptic current in the surface layer of the NBoB. The amplitude of the elliptic current is notably high in the northern and eastern regions of the NBoB and generally flows in a clockwise direction. With the southward movement, the amplitude of the elliptic current decreases, and its direction shifts counterclockwise. The semimajor axis of the tidal ellipse points toward the estuary area to the NE of the NBoB. These results are consistent with the findings of Wan *et al.* (2019). Simpson and Hunter (1974) introduced a method for calculating the tidal mixing parameters using the SH parameter formula or  $K$  in Eq. (4). According to Simpson and Hunter (1974), the value of  $K$  indicates the average intensity of tidal mixing in the water column at a specific location. As the value of  $K$  decreases, either due to decreased water depth  $h_0$  or increased depth-averaged M2 tidal velocity ( $u$ ), tidal mixing becomes stronger. Zhu *et al.* (2013) classified  $K$  parameter values into three categories, i.e., strong tidal mixing for  $K$  values  $< 2.0$ , moderate tidal mixing for  $K$  values between 2.0 and 2.8, and weak tidal mixing for  $K$  values  $> 3$ . Fig. 2d shows the SH parameter calculated from the M2 TC, revealing a decrease in the  $K$  value as it approaches the coast. The most notable decrease in the  $K$  value occurred in the northern and eastern regions of the NBoB, indicating strong tidal mixing in those areas.

### Chl-*a* and tidal data

This study focused on analyzing the influence of tidal cycles on Chl-*a* concentration. Given that the cycle between spring and neap tides occurs for approximately 14 days, the analysis was conducted for 1 month, in this case, January 2022. This approach enabled us to observe two full cycles of spring and neap tides within the month. The methodology involves using hourly data over this 1-month period, which adequately captures the tidal influence on Chl-*a*. Hourly Chl-*a* data were obtained from the geostationary meteorological satellite Himawari-8

### Tidal dynamics and chlorophyll *a* concentration

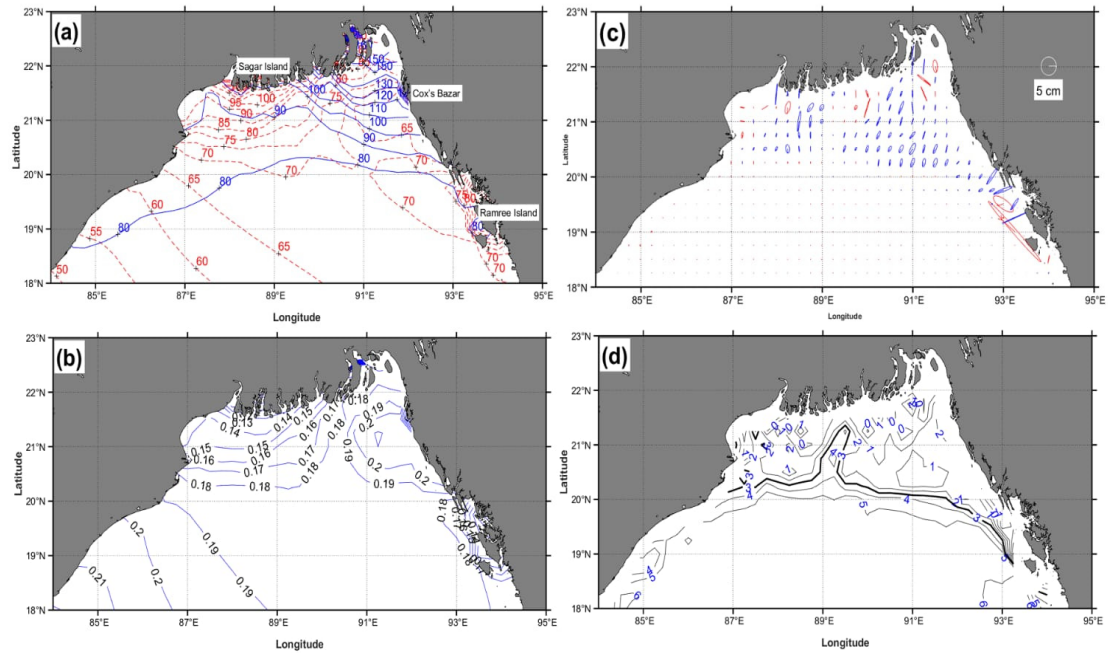


Fig. 2: (a) Amplitude (red dashed line; in centimeters) and M2 phase (blue line; in degrees), (b) tidal type in the NBoB based on the  $F$  value, (c) current ellipses of M2 tides and their orientations (red, clockwise; blue, counterclockwise), and (d) SH parameter  $\log_{10} h/u^3$ .

and provided by the P-Tree System of the JAXA. However, the Chl-*a* data acquired had a significant number of missing values and some outliers, which necessitated interpolation to address these gaps. Therefore, the hourly Chl-*a* data were initially cleaned by filling in missing values and addressing outlier data using extrapolated estimates derived from autoregressive models (Akaike, 1969; Nagahawatte *et al.*, 2023). To elucidate the relationship between Chl-*a* and ROCChl-*a*, derived from Chl-*a*, and their connections with tidal variables, such as SL, TC, and  $|U|$ , these associations are presented in Fig. 3. Fig. 3a shows the time series of Chl-*a* concentrations across three regions: Region 1 is shown in red, Region 2 is shown in blue, and Region 3 is shown in black. Generally, Region 2 exhibits the highest mean Chl-*a* concentrations, followed by Region 3 and Region 1 with the lowest mean Chl-*a* concentrations. Fig. 3b illustrates the ROCChl-*a* for each region, with the corresponding colors of red, blue, and black for Regions 1, 2, and 3, respectively. Notably, the mean ROCChl-*a* values in Region 2 are lower than those in Region 1. This inverse relationship between Chl-*a*

and ROCChl-*a* is understandable when considering their interplay, as expressed in Eq. (3). Consequently, higher Chl-*a* concentrations are associated with lower ROCChl-*a* values. Fig. 3c–3e focus on the tidal variables: SL, TC, and  $|U|$ . Fig. 3c illustrates that Region 2 experiences the highest amplitude of SL, whereas Region 1 experiences the lowest amplitude of SL. A similar pattern is observed with TC, as shown in Fig. 3d, where the highest TC values are in Region 2 and the lowest TC values are in Region 1. This consistency extends to the tidal variable  $|U|$ , with Region 2 exhibiting the highest values and Region 1 exhibiting the lowest values. The interconnectedness of these tidal variables is apparent; a higher SL tends to result in increased values of TC and  $|U|$ . The low values in Region 1 are also reflected in the M2 amplitude values shown in Fig. 2a, with the highest amplitude observed in Region 2. Relating this to the SH parameter values from Fig. 2d, lower SH values correspond to areas with high dynamics, as indicated by the high SL, TC, and  $|U|$  values. A lower SH value in a region indicates higher dynamics and consequently increased mixing. The relationship between Chl-*a*

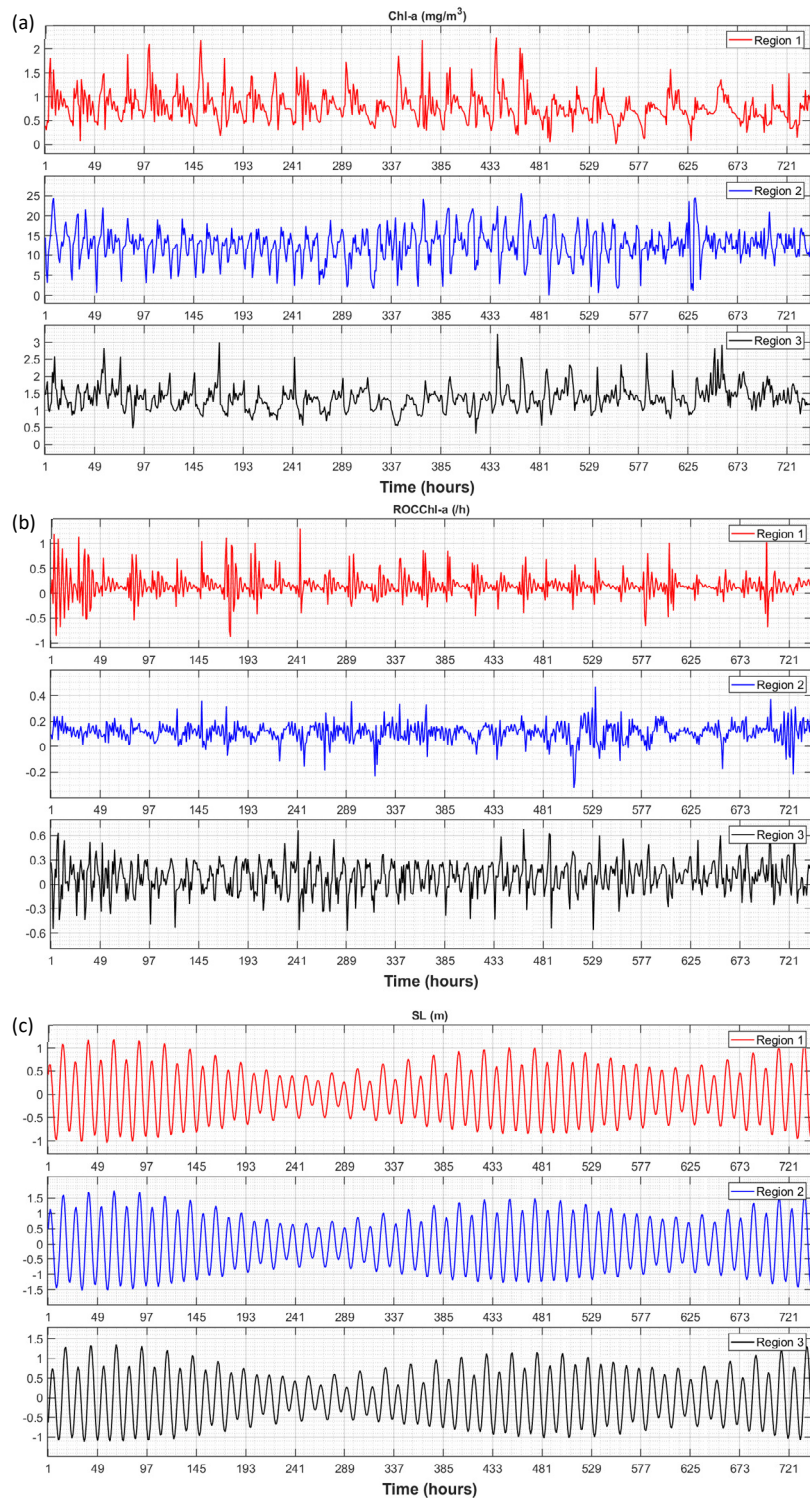
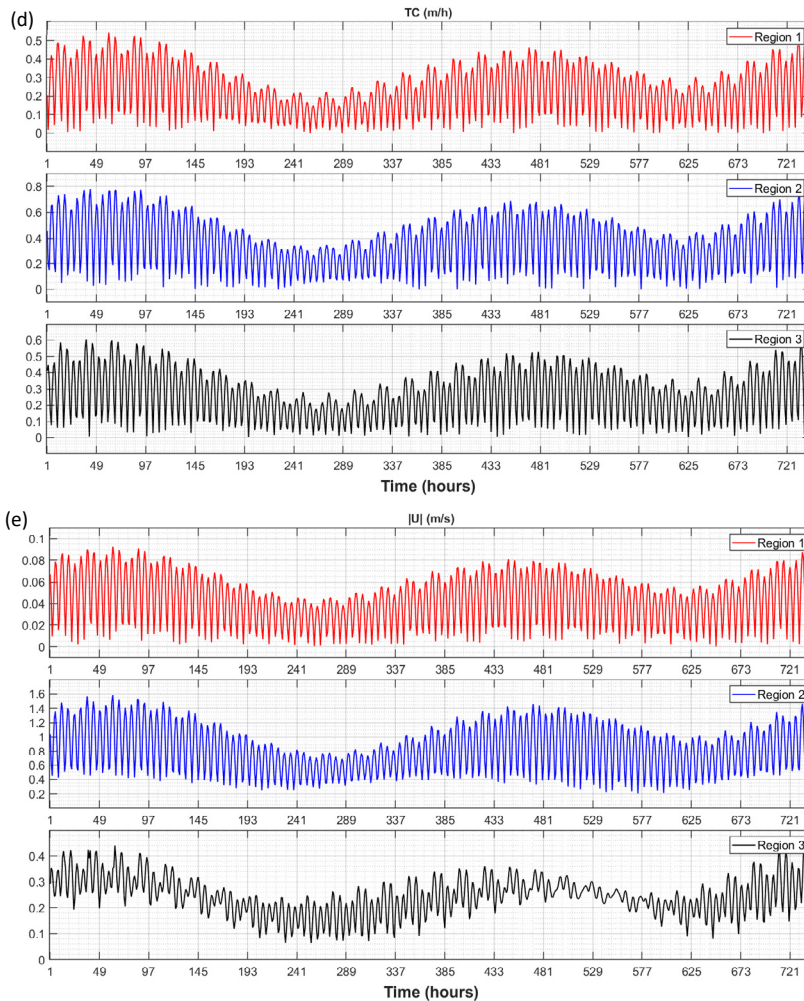


Fig. 3: Time series for (a) Chl-*a*, (b) ROCChl-*a*, (c) SL, (d) TC, and (e)  $|U|$  in Regions 1, 2, and 3. In the legend, red denotes Region 1, blue denotes Region 2, and black denotes Region 3. All time series are for January 2022.



Continued Fig. 3: Time series for (a) Chl- $\alpha$ , (b) ROCCHL- $\alpha$ , (c) SL, (d) TC, and (e)  $|U|$  in Regions 1, 2, and 3. In the legend, red denotes Region 1, blue denotes Region 2, and black denotes Region 3. All time series are for January 2022.

and these three tidal variables is particularly intriguing. Higher SL, TC, and  $|U|$  values correspond to increased Chl- $\alpha$  concentrations. This finding is linked to the SH parameter values shown in Fig. 2d. Regions with higher mixing (indicated by lower SH values) have higher Chl- $\alpha$  concentrations. This finding indicates a dynamic interplay where tidal influences and water column mixing significantly impact Chl- $\alpha$  concentrations.

#### CWT

Fig. 4 shows the results of the CWT analyses of Chl- $\alpha$ , ROCCHL- $\alpha$ , SL, TC, and  $|U|$  across Regions 1, 2, and 3 in January 2022. The CWT delineates areas

of significant wavelet power, indicated by thick black contours that represent a 95 percent (%) confidence level against red noise or AR(1). The cone of influence (COI) in these plots demarcates regions where estimations are more reliable (denoted by bright colors) from those that are less reliable (denoted by pale colors). In Region 1, the CWT of Chl- $\alpha$  reveals significant areas in the 6–12-h band on Days 7 and 19; similarly, significant areas in the 24-h band occur on these same days. Notably, Day 7 marks the end phase of the spring tides, whereas Day 19 corresponds to the occurrence of spring tides. In Region 2, the CWT of Chl- $\alpha$  shows significant areas in the 7–12-h band from Day 1 to Day 26. In addition, significant regions

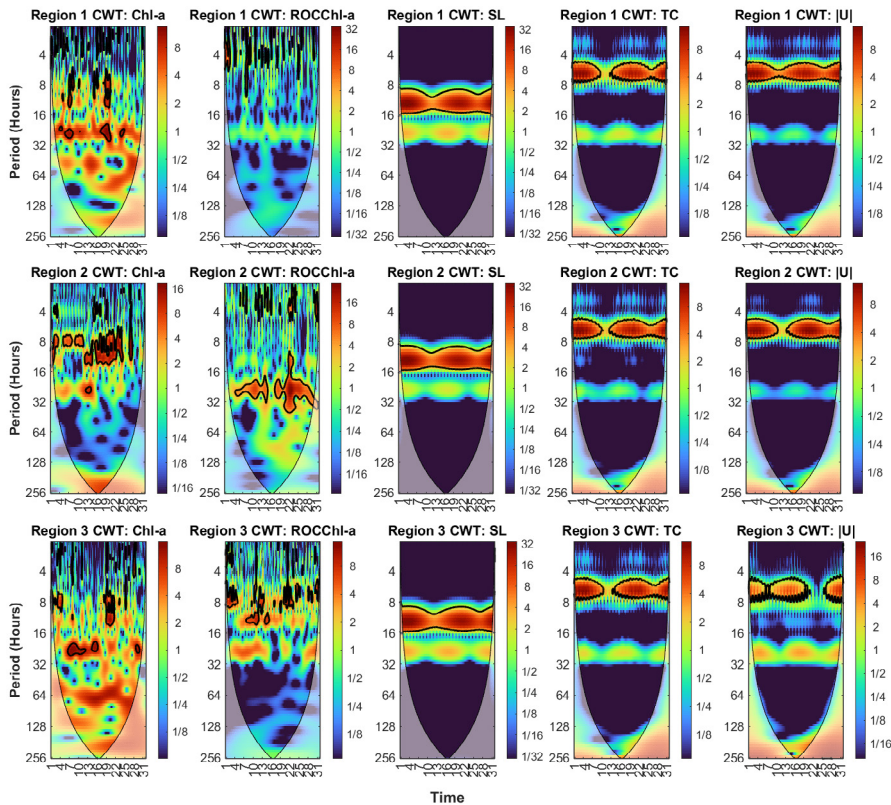


Fig. 4: CWT of Chl- $\alpha$ , ROCChl- $\alpha$ , SL, TC, and  $|U|$  across Regions 1–3 in January 2022. The x-axis represents the time in days, whereas the y-axis represents the period in hours (h). The color bar represents the magnitude of the wavelet coefficients, indicating the strength of the signal components at different time–period points. The thick black contours represent AR(1), whereas COI indicates regions with more reliable estimations (denoted by bright colors) and less reliable estimations (denoted by pale colors).

in the 24-h band were observed on Day 13, coinciding with the initial phase of the spring tides. In Region 3, the CWT of Chl- $\alpha$  indicates significant areas in the 7–12-h band from Day 1 to Day 5 and from Day 18 to Day 22. Significant regions in the 24-h band were evident from Day 7 to Day 16 and on Day 29. The periods from Day 1 to Day 5 and from Day 18 to Day 22 correspond to the occurrence of spring tides, whereas Days 7–16 mark the occurrence of neap tides. The CWT of ROCChl- $\alpha$  in Region 1 shows significant areas in the 1- to 6-h band on Day 2, aligning with the period of spring tides from Day 1 to Day 6. In Region 2, the CWT of ROCChl- $\alpha$  reveals significant areas in the 2–4-h band on Days 23 and 31 and in the 10–40-h band from Day 4 to Day 30, coinciding with the neap tides from Day 23 to Day 31. In Region 3, the CWT of ROCChl- $\alpha$  shows significant areas in the 5–12-h band the entire month. The CWT analyses of SL in Regions 1, 2, and 3

all indicate significant areas in the 8–16-h band from Day 1 to Day 31. This finding is consistent with those of [Blauw et al. \(2012\)](#) in the southern North Sea. Finally, the CWT of TC and  $|U|$  in all three regions reveals significant areas in the 5–7-h band the entire month, highlighting consistent tidal influences across these regions and indicating a robust TC pattern. [Blauw et al. \(2012\)](#) analyzed the CWT of Chl- $\alpha$  in the southern North Sea, an area characterized by semidiurnal tidal patterns, in 2007 and determined that Chl- $\alpha$  exhibited dominant periodicities of approximately 6 h and 12 min, 12 h and 25 min, and 24 h. These periodicities are consistent with the findings of the present study, as shown in [Fig. 4](#), across the three research regions in January 2022. Such similarities in periodicity indicate a consistent pattern in Chl- $\alpha$  variability associated with semidiurnal tides, enhancing the understanding of Chl- $\alpha$  dynamics in areas influenced by these tidal

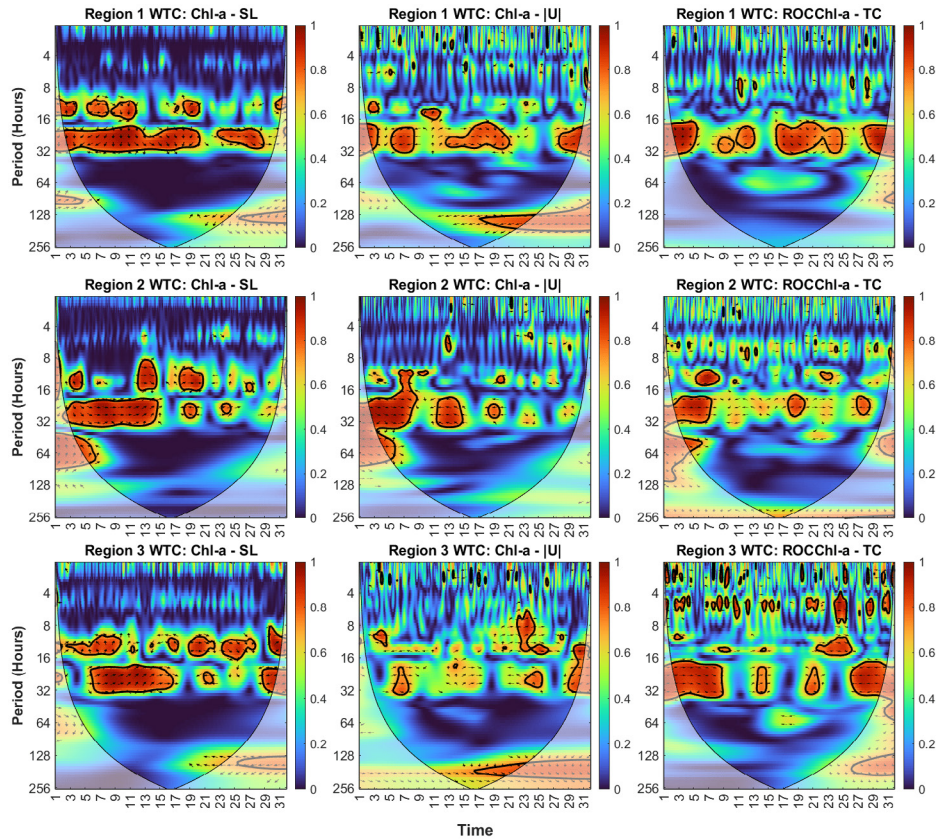


Fig. 5: WTC of Chl-*a* and SL, Chl-*a* and  $|U|$ , and ROCChl-*a* and TC across Regions 1–3 in January 2022. The x-axis represents the time in days, whereas the y-axis represents the period in hours. The color bar represents the coherence values, indicating the degree of correlation between two signals at different time and period scales. The thick black contours represent AR(1), whereas COI indicates regions with more reliable estimations (denoted by bright colors) and less reliable estimations (denoted by pale colors). The arrows represent the phase information between the two signals.

patterns. This consistency is also observed in the SL data. [Blauw et al. \(2012\)](#) noted that SL exhibited a 12-h period, which is consistent with the CWT results of SL shown in [Fig. 4](#), confirming that the findings of the present study are consistent with those of [Blauw et al. \(2012\)](#).

#### WTC

[Fig. 5](#) illustrates the WTC between the time series of Chl-*a* and SL, Chl-*a* and  $|U|$ , and ROCChl-*a* and TC across Regions 1, 2, and 3 in January 2022. For better understanding, an interpretative guide was provided for the WTC results. When conducting WTC analysis between two variables, i.e., A and B, the direction of the arrow within the coherence plot can fall into one of four quadrants, each providing insights into the phase relationship between A and B, as follows: (1) In

Quadrant I, the phase lag  $x$  indicates that A and B are in phase, with B leading. (2) In Quadrant II, the phase lag  $x-\pi$  indicates that A and B are in the antiphase, with A leading. (3) In Quadrant III, the phase lag  $x-\pi$  indicates that A and B are in the antiphase, with B leading. (4) In Quadrant IV, the phase lag  $x$  indicates that A and B are in phase, with A leading. These guidelines are crucial for interpreting the phase relationships between Chl-*a* and SL, Chl-*a* and  $|U|$ , and ROCChl-*a* and TC. These essential insights into the synchronicity or time lag between these two time series at each of the research regions enhance the understanding of the interactions between the Chl-*a* variables and the oceanographic tide data. [Table 2](#) presents a quantitative analysis of the data illustrated in [Fig. 5](#), showing the WTC relationships between

Table 2: WTC between Chl-*a* and SL, Chl-*a* and |*U*|, and ROCChl-*a* and TC

Region	Chl- <i>a</i> and SL			Chl- <i>a</i> and   <i>U</i>			ROCChl- <i>a</i> and TC				
	Period (h)	Time (days)	Phase Lag (deg)	Period (h)	Time (days)	Phase Lag (deg)	Period (h)	Time (days)	Phase Lag (deg)		
1	10-16	2-3	110 <sup>-*</sup>	14-16	9-11	80	16-34	2-6	100 <sup>-</sup>		
		5-7	20		18-32	3		15 <sup>*</sup>	8-10	135 <sup>-*</sup>	
		8-10	110 <sup>-</sup>			5-8		150 <sup>-</sup>	11-13	30	
		18-20	45			13-21		45 <sup>*</sup>	16-21	45 <sup>*</sup>	
		30	30 <sup>*</sup>			27-30		30	22-24	180 <sup>-</sup>	
	20-32	2-10	110 <sup>-</sup>	128-150	17-24	170 <sup>-</sup>		28-30	10		
		11-20	60 <sup>*</sup>								
		23-28	30 <sup>*</sup>								
2	12-16	4	110 <sup>-*</sup>	10-34	2-8	10 <sup>*</sup>	12-15	5-8	150 <sup>-</sup>		
		17-20	0		20-34	11-14		170 <sup>-*</sup>	12	23	150 <sup>-</sup>
	8-16	12-14	10 <sup>*</sup>	24-32	19	180 <sup>-</sup>	20-32	2-9	0		
		2-8	30 <sup>*</sup>		35-70	4-5		0	18-19	10	
	20-34	9-14	30					27-28	180 <sup>-</sup>		
		19	170 <sup>-*</sup>				48-64	4-6	30 <sup>*</sup>		
	24	24	10								
3	10-16	3-8	120 <sup>-*</sup>	12	4	170 <sup>-*</sup>	4-8	23-24	0		
		16	120 <sup>-*</sup>		6-16	22-26		30	6	28	0
		19-21	0		14-32	28-30		150 <sup>-</sup>	4-6	30	90 <sup>*</sup>
		23-27	45 <sup>*</sup>		20-34	5-7		10 <sup>*</sup>	10-16	22-26	20 <sup>*</sup>
		29-30	45		24-32	23-25		150 <sup>-*</sup>	16-34	2-8	20 <sup>*</sup>
	20-32	5-16	30	170-200	17-22	30 <sup>*</sup>		26-30	180 <sup>-</sup>		
		21	180 <sup>-</sup>					20-32	14	30	
		28-30	170 <sup>-</sup>						20-21	90	

Chl-*a* and SL, Chl-*a* and |*U*|, and ROCChl-*a* and TC across Regions 1, 2, and 3 in January 2022.

The WTC findings are visualized with thick black contours representing AR(1), and COI distinguishing between more reliable (denoted by bright colors) and less reliable (denoted by pale colors) estimation regions. WTC analyses of Chl-*a* and SL over periods of 12 and 24 h are conducted. In Region 1, WTC results of Chl-*a* and SL exhibit significant coherence in the 10–16-h and 20–32-h periods. Notable days within the 10–16-h period include the 2nd–3rd, 5th–7th, 8th–10th, 18th–20th, and 30th. Quadrant I arrows on the 5th–7th and 18th–20th indicate a positive correlation with SL leading Chl-*a*, whereas Quadrant II arrows on the 2nd–3rd indicate a negative correlation with Chl-*a* leading SL. Quadrant III arrows on the 8th–10th indicate a negative correlation with SL leading Chl-*a*, whereas Quadrant IV arrows on the 30th indicate a positive correlation with Chl-*a* leading SL. In the 20–32-h period, significant coherence was observed from the 2nd to 10th, 11th to 20th, and 23rd to 28th. Quadrant III arrows on the 2nd–10th indicate a negative correlation with SL leading Chl-*a*, whereas Quadrant IV arrows on the 11th–20th and 23rd–28th

indicate a positive correlation with Chl-*a* leading SL. WTC of Chl-*a* and |*U*| in Region 1 exhibit significant coherence in the 14–16-h, 18–32-h, and 128–150-h periods. In the 14–16-h period, notable coherence is observed on the 9th–11th, with Quadrant I arrows indicating a positive correlation, where |*U*| leads Chl-*a*. In the 18–32-h period, significant coherence is observed on the 3rd, 5th–8th, 13th–21st, and 27th–30th. During the 27th–30th, Quadrant I arrows show a positive correlation, with |*U*| leading Chl-*a*. Conversely, Quadrant III arrows on the 5th–8th show a negative correlation, with |*U*| leading Chl-*a*. Meanwhile, Quadrant IV arrows on the 3rd and 13th–21st show a positive correlation, with Chl-*a* leading |*U*|. In the extended 128–150-h period, significant coherence was observed on the 17th–24th. Here, Quadrant III arrows show a negative correlation, with |*U*| leading Chl-*a*. The WTC results of ROCChl-*a* and TC in Region 1 indicate significant areas in the 16–34-h period. During this period, significance was observed on the 2nd–6th, 8th–10th, 11th–13th, 16th–21st, 22nd–24th, and 28th–30th days. Arrows in Quadrant I on the 11th–13th and 28th–30th days indicate a positive correlation, with TC leading

ROCChl-*a*. Arrows in Quadrant II on the 8th–10th days indicate a negative correlation, with ROCChl-*a* leading TC. Arrows in Quadrant III on the 2nd–6th days indicate a negative correlation, with TC leading ROCChl-*a*. Arrows in Quadrant IV on the 16th–21st days indicate a positive correlation, with ROCChl-*a* leading TC. However, on the 22nd–24th day, ROCChl-*a* and TC exhibited a negative correlation and moved together because of a phase lag of 180°. In Regions 2 and 3, the interpretations are similar to those in Region 1. The quantitative results are shown in [Table 2](#). [Díez-Minguito and de Swart \(2020\)](#) described the WTC between Chl-*a* and  $|U|$  in the Guadalquivir River, which experiences the same semidiurnal tidal pattern as the NBoB. During spring tides, they observed significant WTC between Chl-*a* and  $|U|$  over periods of 6, 12, and 24 h. These findings are consistent with the WTC results of Chl-*a* and  $|U|$ , as shown in [Fig. 5](#). The similarities in significant areas and periodicities between both studies support the relationship between Chl-*a* and  $|U|$  in regions affected by semidiurnal tides. [Blauw et al. \(2012\)](#) also reported significant WTC between ROCChl-*a* and TC in the winter of 2007 in the southern North Sea, which experiences semidiurnal tides similar to the NBoB, and observed significant coherence in periods of 6, 12, and 24 h. These findings are also consistent with the results of the present study, as shown in [Fig. 5](#). The similarities in significant areas in both the CWT and WTC analyses between the current study and the research of [Blauw et al. \(2012\)](#) and [Díez-Minguito and de Swart \(2020\)](#) confirm that the findings of the current study are consistent with those of previous studies.

## CONCLUSION

The NBoB has been categorized based on the  $F$  value, an essential metric for tidal classification, revealing that most areas within the bay have an  $F$  value  $< 0.25$ , indicating a predominantly semidiurnal tidal pattern. Further exploration of the NBoB features has exposed intriguing dynamics, particularly in the surface layer elliptic current M2. In the northern and eastern regions, there is a significant increase in amplitude, with a dominant clockwise flow direction. By contrast, the amplitude reduces and changes to a counterclockwise pattern as one moves southward. The semimajor axis of the tidal ellipse consistently points toward the estuary in

the north and east. The analysis of the SH parameter, derived from M2 TC, shows a marked decrease in its value closer to the coast, particularly in the north and east, indicating enhanced tidal mixing in these areas and a complex interaction of various forces. An examination of the tidal variables reveals a consistent pattern, i.e., Region 2 has the highest amplitude of SL, TC, and  $|U|$ , whereas Region 1 has the lowest amplitude of SL, TC, and  $|U|$ . A significant correlation exists among these variables, with the amplitude of SL being related to increased TC and  $|U|$  values. In addition, the low M2 amplitude observed in Region 1 correlates with a higher SH parameter value. Regions 1 and 2 are characterized by the lowest and highest M2 amplitudes, respectively. Consequently, this results in the highest SH parameter values in Region 1 and the lowest SH parameter values in Region 2. Furthermore, a notable correlation between Chl-*a* concentrations and tidal variables (SL, TC, and  $|U|$ ) was observed. Regions with higher values of these tidal parameters consistently show increased mean Chl-*a* concentrations. This trend is also evident in the SH parameter values, indicating that areas with more intense mixing and dynamic conditions tend to have higher mean Chl-*a* concentrations. The CWT analysis consistently revealed SL fluctuations across all regions within the 8–16-h range throughout the month, emphasizing the ongoing impact of tidal forces on SL. Moreover, both TC and  $|U|$  exhibited uniform tidal influences across all areas, particularly within the 5–7-h band, underscoring the significant influence of tidal dynamics on these hydrodynamic factors. Overall, the CWT analysis has enhanced the understanding of the complex relationships between Chl-*a*, ROCChl-*a*, and tidal variables (SL, TC, and  $|U|$ ) and their interplay with tidal cycles across these regions. The WTC analysis performed on the time series data of Chl-*a* and SL, Chl-*a* and  $|U|$ , as well as ROCChl-*a* and TC at Regions 1, 2, and 3, revealed a significant level of coherence among these variables across all three regions. This coherence was observed over various time intervals, showcasing a spectrum of correlations and phase differences between the parameters. These findings collectively emphasize the complex network of interrelations between these environmental variables. The impact of semidiurnal and diurnal cycles on Chl-*a* is distinctly traceable through the patterns observed in the CWT and WTC figures. Specifically, the semidiurnal influence is

marked by a prominent approximately 12-h periodicity in both CWT and WTC analyses, whereas the diurnal influence is characterized by approximately 24-h periodicity evident in these analyses. The observed variations in coherence, strength of the correlations, and phase lags between them highlight the fluid and dynamic nature of the interactions between Chl-*a*, SL,  $|U|$ , ROCChl-*a*, and TC. The results of the present study, which demonstrate correlations between tidal variables and Chl-*a* concentrations, have significant practical implications in various marine and environmental fields. By understanding the relationship between tidal dynamics and Chl-*a* concentrations, fisheries can optimize their harvesting strategies to ensure the sustainability of fish populations. In addition, these insights are crucial for ecosystem management, as regions with higher tidal parameters (SL, TC, and  $|U|$ ) tend to exhibit increased Chl-*a* concentrations. This knowledge is valuable for marine biologists and environmental scientists in understanding marine food chains and biogeochemical cycles. The findings are particularly relevant to the fishing industry. Understanding the relationship between tidal dynamics and Chl-*a* concentrations can aid in predicting fish population dynamics, leading to more efficient and sustainable fishing practices.

#### AUTHOR CONTRIBUTIONS

M.N. Hidayat performed the literature review, compiled the data, the experiments, analyzed and interpreted the data, prepared the manuscript text, and manuscript edition. R. Wafdan performed the experiments, interpreted the data, prepared the manuscript text, and manuscript edition. M. Ramli performed the literature review, prepared the manuscript text, and manuscript edition. Z.A. Muchlisin performed the literature review, prepared the manuscript text, and manuscript edition. S. Rizal performed the literature review, experimental design, analyzed and interpreted the data, prepared the manuscript text, and manuscript edition.

#### ACKNOWLEDGEMENT

This study was funded by the Ministry of Education and Culture of the Republic of Indonesia under the "Penelitian Profesor" program for the 2021 fiscal year, contract number [7/UN11.2.1/PT.01.03/PNBP/2021], and by the Ministry of Education, Culture, Research,

and Technology of the Republic of Indonesia under the "Penelitian Pendidikan Magister menuju Doktor untuk Sarjana Unggul" program for the 2023 fiscal year, contract number [587/UN11.2.1/PT.01.03/DPRM/2023].

#### CONFLICT OF INTEREST

The authors declare that there is no conflict of interests regarding the publication of this manuscript. In addition, the ethical issues, including plagiarism, informed consent, misconduct, data fabrication and/or falsification, double publication and/or submission, and redundancy have been completely observed by the authors.

#### OPEN ACCESS

©2024 The author(s). This article is licensed under a Creative Commons Attribution 4.0 International License, which permits use, sharing, adaptation, distribution and reproduction in any medium or format, as long as you give appropriate credit to the original author(s) and the source, provide a link to the Creative Commons license, and indicate if changes were made. The images or other third-party material in this article are included in the article's Creative Commons license, unless indicated otherwise in a credit line to the material. If material is not included in the article's Creative Commons license and your intended use is not permitted by statutory regulation or exceeds the permitted use, you will need to obtain permission directly from the copyright holder. To view a copy of this license, visit: <http://creativecommons.org/licenses/by/4.0/>

#### PUBLISHER'S NOTE

GJESM Publisher remains neutral with regard to jurisdictional claims in published maps and institutional affiliations.

#### ABBREVIATIONS

%	Percent
°N	Degrees North
°E	Degrees East
$\psi_o$	Morlet wavelet function
$\omega_o$	Dimensionless frequency
$\delta_t$	Uniform time intervals
$\phi_n(s)$	Phase angle

$\Im$	Imaginary part operator	$S_2$	Principal solar semidiurnal constituent
$\Re$	Real part operator	$S.D.$	Standard deviation
$AR(1)$	Autoregressive model of order 1	$SH$	Simpson-Hunter parameter
$Chl-a$	Chlorophyll-a	$parameter$	
$cm$	Centimeters	$SL$	Sea level
$COI$	Cone of influence	$SPM$	Suspended particulate matter
$CWT$	Continuous wavelet transform	$SRTM15+$	Shuttle Radar Topography Mission 15 plus
$deg$	Degree	$SSS$	Sea surface salinity
$Eq.$	Equation	$SST$	Sea surface temperature
$F$	Formzahl Number	$SW$	Southwest
$FFT$	Fast Fourier Transform	$t$	time
$h$	Hour	$TC$	Tidal current
$h_o$	Average water depth	$TMD$	Tidal Model Driver
$/h$	One per hour	$u$	Depth-average tidal velocity (M2)
$IQR$	Interquartile	$ U $	Current's magnitude
$JAXA$	Japan Aerospace Exploration Agency	$WTC$	Wavelet transform coherence
$K1$	Lunisolar diurnal constituent		
$km$	Kilometer		
$ln$	Natural logarithm		
	Logarithm with base 10		
$log_{10}$			
$m$	Meter		
$m/h$	Meter per hour		
$m/s$	Meter per second		
$M_2$	Lunar Semidiurnal Tide		
$mg/m^3$	Milligrams per cubic meter		
$Max$	Maximum		
$Min$	Minimum		
$min$	Minute		
$MODIS$	Moderate resolution imaging spectroradiometer		
$n$	Reversed time index		
$N$	Natural number		
$NBoB$	Northern Bay of Bengal		
$NE$	Northeast		
$O_1$	Lunar diurnal constituent		
$ROChl-a$	Rate of change chlorophyll-a		
$s$	Wavelet scale		
$S$	Smoothing operator		

## REFERENCES

- Akaike, H., (1969). Fitting autoregressive models for prediction. In Selected Papers of Hirotugu Akaike. NY: Springer New York, New York.
- Alsalia, N.; Haditjar, Y.; Wafdan, R.; Ikhwan, M.; Chaliluddin, M.A.; Sugianto, S.; Rizal, S., (2022). The currents, sea surface temperature, and salinity patterns in the Bay of Bengal. E3S Web Conference. 339: 1-7 (**7 pages**).
- Azhikodan, G.; Yokoyama, K., (2016). Spatio-temporal variability of phytoplankton (Chlorophyll-a) in relation to salinity, suspended sediment concentration, and light intensity in a macrotidal estuary. Cont. Shelf Res., 126: 15-26 (**12 pages**).
- Blauw, A. N.; Beninca, E.; Laane, R. W.; Greenwood, N.; Huisman, J., (2012). Dancing with the tides: fluctuations of coastal phytoplankton orchestrated by different oscillatory modes of the tidal cycle. PLoS One, 7(11): 1-14 (**14 pages**).
- Cadier, M.; Gorgues, T.; LHelguen, S.; Sourisseau, M.; Memery, L., (2017). Tidal cycle control of biogeochemical and ecological properties of a macrotidal ecosystem. Geophys. Res. Lett., 44(16): 8453-8462 (**10 pages**).
- Cullen, J.J.; Lewis M.R., (1988). The kinetics of algal photoadaptation in the context of vertical mixing. J. Plankton Res., 10(5): 1039–1063 (**25 pages**).
- Demers, S.; Legendre, L.; Therriault, J.C., (1986). Phytoplankton responses to vertical tidal mixing, in Tidal Mixing and Plankton Dynamics, Springer, New York. 1–40 (**40 pages**).
- Díez-Minguito, M.; de Swart, H.E., (2020). Relationships Between Chlorophyll-a and Suspended Sediment Concentration in a High-Nutrient Load Estuary: An Observational and Idealized Modeling Approach. J. Geophys. Res., C, 125(3): 1-21 (**21 pages**).
- Eleveld, M. A.; Van der Wal, D.; Van Kessel, T., (2014). Estuarine

- suspended particulate matter concentrations from sun-synchronous satellite remote sensing: tidal and meteorological effects and biases. *Remote Sens. Environ.*, 143: 204–215 **(12 pages)**.
- FAO, (2011). Aquaculture department. Global aquaculture production statistics for the year.
- Fu, C., James, A.L.; Wachowiak, M.P., (2012). Analyzing the combined influence of solar activity and El Niño on streamflow across southern Canada. *Water Resour. Res.*, 48(5): 1-19 **(19 pages)**.
- Goswami, B.N.; Rao, S.; Sengupta, D.; Chowdary, S., (2016). Monsoons to mixing in the Bay of Bengal: multiscale air-sea interactions and monsoon predictability. *Oceanography*. 29(2): 18–27 **(10 pages)**.
- Grinsted, A.; Moore, J.C.; Jevrejeva, S., (2004). Application of the cross wavelet transform and wavelet coherence to geophysical time series. *Nonlinear Process Geophys.*, 11(5/6): 561-566 **(6 pages)**.
- Haditjar, Y.; Putri, M.R.; Ismail, N.; Muchlisin, Z.A.; Ikhwan, M.; Rizal, S., (2020). Numerical study of tides in the Malacca Strait with a 3-D model. *Heliyon*, 6(9): 1-16 **(16 pages)**.
- Hidayat, M.N.; Wafdan, R.; Ramli, M.; Muchlisin, Z.A.; Rizal, S., (2023). Relationship between chlorophyll-a, sea surface temperature, and sea surface salinity. *Global J. Environ. Sci. Manage.*, 9(3): 389-402 **(14 pages)**.
- Ikhwan, M.; Wafdan, R.; Haditjar, Y.; Ramli, M.; Muchlisin, Z.A.; Rizal, S., (2021). Simulation and analysis of marine hydrodynamics based on the El Niño scenario. *Global J. Environ. Sci. Manage.*, 7(4): 543-554 **(12 pages)**.
- Koh, C.H.; Khim, J.S.; Araki, H.; Yamanishi, H.; Mogi, H.; Koga, K., (2006). Tidal resuspension of microphytobenthic chlorophyll a in a Nanaura mudflat, Saga, Ariake Sea, Japan: flood–ebb and spring–neap variations. *Mar. Ecol. Prog. Series* 312: 85–100 **(16 pages)**.
- Koropitan, A.F.; Khaldun, M.H.I.; Naulita, Y., (2022). Impact of tropical Cyclone Marcus on ocean subsurface and surface layers. *Global J. Environ. Sci. Manage.*, 8(3): 353-368 **(12 pages)**.
- Kristoufek, L., (2015). What are the main drivers of the Bitcoin price? Evidence from wavelet coherence analysis. *PLoS one*, 10(4): 1-15 **(15 pages)**.
- Krumme, U.; Brenner, M.; Saint-Paul, U., (2008). Spring-neap cycle as a major driver of temporal variations in feeding of intertidal fishes: evidence from the sea catfish *Sciades herzbergii* (Ariidae) of equatorial west Atlantic mangrove creeks. *J. Exp. Mar. Biol. Ecol.* 367: 91–99 **(9 pages)**.
- Lagadeuc, Y.; Brylinski, J.M.; Aelbrecht, D., (1997). Temporal variability of the vertical stratification of a front in a tidal Region Of Freshwater Influence (ROFI) system, *J. Mar. Syst.*, 12(1), 147–155 **(9 pages)**.
- Lauria, M.L.; Purdie, D.A.; Sharples J., (1999). Contrasting phytoplankton distributions controlled by tidal turbulence in an estuary, *J. Mar. Syst.*, 21(1): 189–197 **(9 pages)**.
- Li, J.; Jiang, F.; Wu, R.; Zhang, C.; Tian, Y.; Sun, P.; Yu, H.; Liu, Y.; Ye, Z.; Ma, S.; Liu, S., (2021). Tidally induced temporal variations in growth of young-of-the-year Pacific cod in the Yellow Sea. *J. Geophys. Res. Oceans*. 126:e2020JC016696 **(16 pages)**.
- Madhupratap, M.; Gauns, M.; Ramaiah, N.; Kumar, S.P.; Muraleedharan, P.M.; De Sousa, S.N.; Sardesai, S.; Muraleedharan, U., (2003). Biogeochemistry of the Bay of Bengal: physical, chemical and primary productivity characteristics of the central and western Bay of Bengal during summer monsoon 2001. *Deep Sea Res. Part II Top. Stud. Oceanogr.*, 50(5): 881-896 **(16 pages)**.
- Murakami, H., (2016). Ocean color estimation by Himawari-8/AHI. In *Remote sensing of the oceans and inland waters*. Tech. Appl. Challenges, 9878: 177-186 **(10 pages)**.
- Nagahawatte, N.D.; Paskaranandavivel, N.; Bear, L.R.; Avci, R.; Cheng, L.K., (2023). A novel framework for the removal of pacing artifacts from bio-electrical recordings. *Comput. Biol. Med.*, 155: 1-11 **(11 pages)**.
- Naderipour, A.; Abdul-Malek, Z.; Nowdeh, S.A.; Kamyab, H.; Ramtin, A.R.; Shahrokhi, S.; Klemeš, J.J., (2021). Comparative evaluation of hybrid photovoltaic, wind, tidal and fuel cell clean system design for different regions with remote application considering cost. *J. Clean. Prod.*, 283: 124207 **(12 pages)**.
- Padman, L.; Erofeeva, S., (2005). Tide model driver (TMD) manual. Earth and Space Research.
- Poddar, S.; Chacko, N.; Swain, D., (2019). Estimation of Chlorophyll-a in northern coastal Bay of Bengal using Landsat-8 OLI and Sentinel-2 MSI sensors. *Front. Mar. Sci.* 6: 598 **(11 pages)**.
- Polagye, B.L., (2009). Hydrodynamic effects of kinetic power extraction by in-stream tidal turbines. University of Washington.
- Rahman, M. J.; Cowx, I. G., (2006). Lunar periodicity in growth increment formation in otoliths of hilsa shad (*Tenualosa ilisha*, Clupeidae) in Bangladesh waters. *Fish. Res.*, 81: 342–344 **(3 pages)**.
- Raju, R.M.; Nayak, R.K.; Mulukutla, S.; Mohanty, P.C.; Manche, S.S.; Seshasai, M.V.R.; Dadhwal, V.K., (2022). Variability of the thermal front and its relationship with Chlorophyll-a in the north Bay of Bengal. *Reg. Stud. Mar. Sci.*, 56: 1-12 **(12 pages)**.
- Roden, C. M., (1994). Chlorophyll blooms and the spring/neap tidal cycle: observations at two stations on the coast of Connemara, Ireland. *Mar. Biol.*, 118: 209–213 **(5 pages)**.
- Sharples, J.; Tweddle, J.F.; Mattias Green, J.A.; Palmer, M.R.; Kim, Y.N.; Hickman, A.E.; Holligan, P.M.; Moore, C.M.; Rippeth, T.P.; Simpson, J.H.; Krivtsov, V., (2007). Spring-neap modulation of internal tide mixing and vertical nitrate fluxes at a shelf edge in summer. *Limnol. Oceanogr.*, 52: 1735–1747 **(14 pages)**.
- Shi, W.; Wang, M.; Jiang, L., (2011). Spring-neap tidal effects on satellite ocean color observations in the Bohai Sea, Yellow Sea, and East China Sea. *J. Geophys. Res. Oceans* 116: C12 **(13 pages)**.
- Shi, W.; Wang, M.; Jiang, L., (2013). Tidal effects on ecosystem variability in the Chesapeake Bay from MODIS-Aqua. *Remote Sens. Environ.*, 138: 65–76 **(12 pages)**.
- Simpson, J.H.; Hunter, J.R., (1974). Fronts in the Irish sea. *Nature*. 250(5465): 404-406 **(3 pages)**.
- Sindhu, B.; Unnikrishnan, A.S., (2013). Characteristics of tides in the Bay of Bengal. *Mar. Geod.*, 36(4): 377-407 **(31 pages)**.
- Tazkia, A.R.; Krien, Y.; Durand, F.; Testut, L.; Islam, A. S.; Papa, F.; Bertin, X., (2017). Seasonal modulation of M2 tide in the Northern Bay of Bengal. *Cont. Shelf Res.*, 137: 154-162 **(9 pages)**.
- Torrence, C.; Compo, G.P., (1998). A practical guide to wavelet analysis. *Bull. Am. Meteorol. Soc.*, 79 (1): 61–78 **(18 pages)**.
- Van der Hout, C. M.; Witbaard, R.; Bergman, M. J. N.; Duineveld, G. C. A.; Rozemeijer, M. J. C.; Gerckema, T., (2017). The dynamics of suspended particulate matter (SPM) and chlorophyll-a from intratidal to annual time scales in a coastal turbidity maximum. *J. Sea Res.*, 127: 105–118 **(14 pages)**.

Wan, W.; Feng, X.; Liu, Q.; Yin, B.; Yang, D.; Gao, G., (2019). Study of the tide and tidal currents in the Bay of Bengal based on refined simulations. *J. Coast. Res.*, 35(1): 33-40 (8 pages).  
Wolanski, E.; Elliott, M., (2015). *Estuarine ecology: an introduction*. Elsevier, Amsterdam.  
Xing, Q.; Yu, H.; Yu, H.; Wang, H.; Ito, S. I.; Yuan, C., (2021). Evaluating

the Spring-Neap Tidal Effects on Chlorophyll-a Variations Based on the Geostationary Satellite. *Front. Mar. Sci.*, 8: 758538 (12 pages).  
Zhu, J.; Hu, J.; Liu, Z., (2013). On summer stratification and tidal mixing in the Taiwan Strait. *Front. Earth Sci.*, 7: 141-150 (10 pages).

#### AUTHOR (S) BIOSKETCHES

**Hidayat, M.N.**, Ph.D. Candidate, Graduate School of Mathematics and Applied Sciences, Universitas Syiah Kuala, Banda Aceh 23111, Indonesia.

- Email: [muh.nurhidayat@usk.ac.id](mailto:muh.nurhidayat@usk.ac.id)
- ORCID: 0000-0001-8727-3615
- Web of Science ResearcherID: NA
- Scopus Author ID: 58104700300
- Homepage: <https://dmas.usk.ac.id/>

**Wafdan, R.**, M.Mat., Department of Mathematics, Universitas Syiah Kuala, Banda Aceh 23111, Indonesia.

- Email: [wafdan111@usk.ac.id](mailto:wafdan111@usk.ac.id)
- ORCID: 0000-0001-5574-7089
- Web of Science ResearcherID: NA
- Scopus Author ID: 57191094408
- Homepage: <https://fsd.usk.ac.id/wafdan/>

**Ramli, M.**, Ph.D., Professor, Department of Mathematics, Universitas Syiah Kuala, Banda Aceh 23111, Indonesia.

- Email: [marwan.math@usk.ac.id](mailto:marwan.math@usk.ac.id)
- ORCID: 0000-0003-1225-9063
- Web of Science ResearcherID: A-2686-2017
- Scopus Author ID: 57217110324
- Homepage: <https://fsd.usk.ac.id/marwanramli/>

**Muchlisin, Z.A.**, Ph.D., Professor, Department of Aquaculture, Faculty of Marine and Fisheries, Universitas Syiah Kuala, Banda Aceh 23111, Indonesia.

- Email: [muchlisinza@usk.ac.id](mailto:muchlisinza@usk.ac.id)
- ORCID: 0000-0002-0858-1853
- Web of Science ResearcherID: E-2317-2015
- Scopus Author ID: 55937322900
- Homepage: <https://fsd.usk.ac.id/muchlisinza/>

**Rizal, S.**, Ph.D., Professor, Department of Marine Sciences, Faculty of Marine and Fisheries, Universitas Syiah Kuala, Banda Aceh, 23111, Indonesia.

- Email: [srizal@usk.ac.id](mailto:srizal@usk.ac.id)
- ORCID: 0000-0003-3637-2351
- Web of Science ResearcherID: V-7627-2017
- Scopus Author ID: 57211267611
- Homepage: [https://fsd.usk.ac.id/syamsul\\_rizal/](https://fsd.usk.ac.id/syamsul_rizal/)

#### HOW TO CITE THIS ARTICLE

Hidayat, M.N.; Wafdan, R.; Ramli, M.; Muchlisin, Z.A.; Rizal, S., (2024). *Patterns and wavelet coherence analysis of tidal dynamics and chlorophyll a concentration*. *Global J. Environ. Sci. Manage.*, 10(3): 1-18.

DOI: [10.22035/gjesm.2024.03.\\*\\*\\*](https://doi.org/10.22035/gjesm.2024.03.***)

URL: \*\*\*

